https://doi.org/10.5194/nhess-2021-101
Preprint. Discussion started: 13 April 2021

Natural Hazards and Earth System Sciences
Discussions

Monitoring and analysis of Woda landslide stability (China) combined with InSAR, GNSS and meteorological data

Bingquan Li [1], Wenliang Jiang [1*], Yongsheng Li [1], Yi Luo [1], Haitao Qian [1], Yanchao Wang [1], Qisong Jiao [1], Qingyun Zhang [2], Zihan Zhou [1], Jingfa Zhang [1]

[1]National Institute of Natural Hazards, Ministry of Emergency Management of China, Beijing, China;
[2]The First Monitoring and Application Centre, China Earthquake Administration, Tianjin, China.

Correspondence to: Jiang_wenliang@163.com

Abstract: Detecting the slow motions of high and distant landslides in remote mountain areas has always been a problem. This paper takes the Woda landslide along the Jinsha River as an example to monitor landslide movement. Although some parts of the landslide body have been found to have moved in recent years, the timing and magnitude of motion have not been systematically monitored or interpreted. Here, we apply the SBAS time series strategy using 65-scene Sentinel-1A/B satellite InSAR images and study the spatial distribution and temporal behaviour of landslide movements between July 4, 2018, and August 29, 2020. Our research results show that the cumulative deformation on the left side of the landslide body with concentrated deformation was approximately 200 mm during the 2-year observation period. By calculating the relationship between the InSAR time series and the precipitation around the landslide, it is found that the landslide deformation is closely related to rainfall. GNSS technology is also deployed on the landslide mass and effectively complements InSAR technology. Simultaneously, based on the results of field surveys and hydrological data analysing the landslide's spatial deformation characteristics and deformation factors, the landslide deformation can also be inferred to be related to precipitation. The method used in this paper can be used for early recognition and early warning of high and remote landslides.

1 Introduction

Based on a synthesis of previous studies and the Kumamoto seismic data, this paper uses a combination of multiple interferometric synthetic aperture radar (InSAR) techniques and multisource data inversion methods to analyse the 3D deformation field of the Kumamoto earthquake. Through comparative analysis, the joint analysis of multisource data is found to improve the calculation accuracy of the 3D deformation field and provide a reference for further study of source parameters and fault geometric kinematics. According to the 2019 National Geological Hazard Bulletin of the China Geological and Environmental Supervision Institute, landslides and debris flows accounted for 88.3% of the total number of geological disasters. At the same time, with the continuous advancement of China's economic development, large-scale engineering projects such as urbanization, railways, and nuclear and hydroelectric power plants continue to increase in number, and the economic threat from geological disasters is increasing (Chen et al., 2011). Because some landslides have the characteristics of "high position" and "concealment", they are difficult to identify by the naked eye and traditional means; dammed lakes are easily formed, and the economic losses and casualties that result are difficult to estimate. Two large-scale landslides and river blockage incidents in Baige village, Boluo township, Jiangda County, Tibet, in October 2018 and November 2018 are taken as examples. Landslide barriers blocking rivers cause heavy losses of life and property and have attracted widespread attention from society and the government (Li et al., 2019). The occurrence of two landslide dams blocking the river has increased the need for people to identify potential catastrophic landslide disasters in mountainous areas, analyse the factors that possibly induce them, and further assess related risks.

https://doi.org/10.5194/nhess-2021-101
Preprint. Discussion started: 13 April 2021


Natural Hazards and Earth System Sciences Discussions

Landslides are slope failures in response to an increased ratio of destabilizing shear stress to resisting shear strength (Hu et al., 2016). It is generally believed that changes in external physical factors, such as heavy rainfall or rapid snow melting (increase in pore pressure) (Iverson et al., 2000), ground shaking (earthquakes or volcanic eruptions) (Malamud et al., 2000), ecological events (wildfires) (Cannon et al., 2001), atmospheric tides (Schulz et al., 2009) and anthropogenic activities (Highland et al., 2008) can induce landslides. More than 70% of the geological disasters that cause catastrophic consequences are within the range of known hidden danger points for such disasters. The main reason is that the disaster sources are located in the middle of mountains, and most areas are inaccessible and covered by vegetation. Given the characteristic concealment, however, traditional manual investigations and group defences are powerless in the face of these disasters, and it is difficult for traditional methods to detect hidden dangers of such disasters in advance. Since the early 1990s, InSAR techniques have measured cm- to mm-level deformation in various geodynamic settings (Simons et al., 2007). SAR technology has been proven to be very effective for detecting landslides along the Jinsha River (Yin et al., 2006). The InSAR method can provide key information about the location, boundary and movement of a landslide (Schlögel et al., 2015; Sun et al., 2015). InSAR technology can obtain a wide range of surface deformation, but this technology also has shortcomings such as a long revisit period and low spatial-temporal resolution. Therefore, this work also established global navigation satellite system (GNSS) sites on the landslide body. Although the deformation results obtained represent discrete point deformation, GNSS technology is characterized by high-precision, quasi-real-time continuous monitoring, which effectively complements the advantages of InSAR technology. In this work, we applied time series InSAR technology and GNSS to the Woda landslide, combined with field surveys and hydrological data, and systematically analysed the causal factors and spatial distribution characteristics of Woda landslide deformation.

2 Geological setting

2.1 Geological setting of the Woda landslide

In terms of regional structure, according to the literature (Zhou et al., 2008), the location of the Woda landslide belongs to the Jiangda structural belt in eastern Tibet. The Jiangda structural belt is located in the northern section of the Sanjiang structural belt in Southwest China on the eastern margin of the Changdu block and on the western side of the Jinshajiang ancient suture zone and is bounded by the Zixiasi-Deqinsi fault and the Jinshajiang fault (Figure 1). The Jiangda structural belt is derived from the ocean-continental volcanic arc system and has undergone transformations involving various structural systems, such as continental-continent collision and welding, intracontinental rifting, and intracontinental orogenesis. Under the intracontinental orogenic strike-slip regime, the Jiangda structural belt is mainly restricted by strike-slip movement along the Jinshajiang fault. In terms of the structure of a small area, the structure of the Woda landslide is shown in Figure 2. Figure 2 illustrates that the rock formations around the Woda landslide are changeable. The landslide and its surrounding areas are speculated to develop small fold uplift structures. According to data from the literature (Guan et al., 2018), Changdu city, where the landslide is located, is located in an area within the Sanjiang River basin where seismic fault zones are frequently active.

According to the analysis of image data, the landslide body overall has the shape of a circular chair, and the regional geomorphology is a typical plateau alpine valley area. The terrain is inclined from northwest to southeast in the valley of the Jinsha River basin. The features of the landforms in the landslide area (Figure 3) indicate that the elevation of the Jinsha River in the front is approximately 2900 m, the highest elevation at the rear is approximately 3970 m, and the relief is approximately 1000 m. The terrain in the area is relatively high in elevation, the terrain is steep, and the slopes of the mountains are generally

https://doi.org/10.5194/nhess-2021-101
Preprint. Discussion started: 13 April 2021


Natural Hazards and Earth System Sciences Discussions

greater than 30°. Connecting directly to the Jinsha River are many valleys of varying sizes. A relatively large valley has developed in the upper and lower reaches of the landslide body, especially in the upstream area, which is deeply cut; the middle valley is smaller in scale. The front edge of the landslide body has a steep slope; the middle and front parts form a steep slope with abundant trees; the middle part and the upstream and downstream sides of the front part have large undulations in terrain, mostly steep slopes where trees and plants grow luxuriantly; the middle part is a gentle slope platform, which consists of mainly cultivated land where trees grow sporadically; the back is the ancient landslide source area, where trees grow prolifically. On the landslide body, steep landslide ridges are generally developed, especially in the middle and front parts, where steep ridges are dense.

Jiangda County, where the landslide is located, has a plateau continental climate with large annual average temperature differences; the highest temperature is 28°C, the lowest temperature is -15°C, and the annual average temperature is 4.5°C. The average temperature in January is -5°C, and the average temperature in July is 13.2°C. The frost-free period averages 60-80 days, the daily average temperature is above 5°C for 150-170 days, and the daily average temperature is above 0°C for 200-250 days. The average annual precipitation is 549 mm, the sunshine time is long, the annual temperature difference is small, and the daily temperature difference is large. The dry season and the rainy season are distinct, with rain and heat in the same season; rainfall is relatively concentrated from June to September.

2.2 Landslide history

There have been traces of sliding in the history of the Woda landslide, which may represent an accumulation of ancient landslides (collapses). In the middle and rear parts of the landslide body, there are cascading ridges, as shown in Figure 4. The ridges are tens of centimetres to several metres in height, and cross-cutting landslides have developed, extending from tens to hundreds of metres, with varying sizes. This kind of gradual development produces steep ridges that gradually decrease in height from the inside to the outside of the slope; at the rear of the entire landslide body, there is no reverse steep ridge (the slope continues to the outside of the slope). The upper part of the ridge is relatively gentle and overgrown with trees, indicating that this ridge formed earlier than other ridges and remained stable for a long time. According to interviews, the inhabitants of landslide-affected Woda village have lived there for generations. The villagers' responses state that there has never been a house crack due to sliding. In the middle and upper parts of the landslide, although houses have been damaged and abandoned, according to villagers, this deterioration occurred because the residents moved to Lhasa and other cities and their empty houses fell into disrepair, rather than being damaged by sliding.

3 Data and methodology

3.1 Data preparation

We collected 66 scene C-band Sentinel-1A/B ascending data acquired between July 2019 and August 2020 (Figure 5(a)). Compared to other SAR missions, the short revisit times (12 days or 6 days) and short baselines (Figure 6) make InSAR applications promising. This mission has wider coverage (up to 250 km) than previous SAR sensors. We also processed L-band ALOS PALSAR-2 data. However, the long time interval and thick vegetation cover that occur in the study area make coherence difficult to maintain. At the same time, we also set up GNSS sites on the landslide body. As shown, the statistics for GNSS deformation from July 2019 to August 2020 are used mainly to verify the factors of landslide deformation and the

https://doi.org/10.5194/nhess-2021-101
Preprint. Discussion started: 13 April 2021


Natural Hazards and Earth System Sciences Discussions

accuracy of InSAR time series monitoring. Due to equipment issues, the data quality for sites G2 and G4 is poor, and the data from these two sites are not used in this article. Finally, we collected rainfall data from the Dege weather station 50 km from the landslide body, i.e., daily precipitation data from July 2018 to August 2020, to verify whether the landslide deformation was related to precipitation.

3.2 Interferometric processing

Localized large movements of and heavy vegetation on the Woda landslide lead to difficulty in phase unwrapping. Therefore, we needed to carefully consider the number of looks and the window size of the filters applied to interferograms. A large number of looks reduces phase noise but at the cost of lower resolution. A larger window size of filters smooths the fringes but may cause loss of detail at fringe boundaries. In our study, we applied 4 looks in the range (i.e., ~m ground range pixel spacing) and 1 look in the azimuth (i.e., ~25 m azimuth pixel spacing). Interferograms were generated using the GAMMA software. To improve the computational efficiency of Sentinel-1 SAR interferometric calculations based on the existing interferometric processing methods, for the key time-consuming steps (registration, resampling and ESD estimation), a graphics processing unit (GPU)-assisted processing algorithm framework was constructed (Yu et al., 2019) to solve the problem of slow data interference processing efficiency.

Original interferograms may experience a mixture of topography-correlated and turbulent atmospheric errors, manifesting as either short- or long-wavelength signals and degrading spatial-temporal filters when extracting deformation signals by InSAR time series analysis (Yu et al., 2018). Typical spatial and temporal changes of 20% in water vapour have been reported to lead to 10- to 14-cm errors in SIR-C/X-SAR-derived displacements, which is large enough to mask actual ground motions caused by a landslide. Therefore, the atmospheric water vapour delay should not be ignored. We also applied a polynomial function to estimate the orbital ramps based on the unwrapped interferograms processed by the GAMMA minimum-cost-flow module. In addition, we applied a linear polynomial function using those pixels with coherence larger than 0.35 and not located in areas with potential motion for each selected interferometric pair.

3.3 Time series InSAR analysis

Traditional D-InSAR technology is susceptible to the influences and limitations of the time baseline and the atmosphere during processing, which cause certain errors in the deformation results. The application of time series InSAR technology reduces the effects of temporal decoherence, spatial decoherence and atmospheric phases. Among them, Small Baseline Subset (SBAS)-InSAR (Hooper, 2008) technology can yield better results with less data and is widely used in the field of deformation monitoring (Yang et al., 2014; Zhao et al., 2019; Bayer et al., 2017). The actual processing of SBAS-InSAR data is divided into the following three main steps (Figure 7): 1) generation of all the interferograms; 2) removal of the residual errors; and 3) SBAS time series analysis. The specific process is as follows: $N+1$ SAR images arranged in the same area in time sequence $t_0, \dots, t_N$ are obtained; one of them is selected as the main image, and the other SAR images are registered to the main image. $N+1$ SAR images generate M interferograms. Note that each differential interferogram after unwrapping needs to be corrected absolutely with respect to a certain stable region or a reference pixel with known deformation in the figure. Spatial baseline and temporal baseline thresholds are set to construct a small baseline dataset of radar images. Differential interference processing is based on a small baseline dataset and mainly includes removal of the flat ground effect, interferogram filtering and phase unwrapping. For the j-th differential interferogram generated from the SAR image obtained from the image t_A and the main image $t_B (t_B > t_A)$, the interference phase of the pixel with the azimuth coordinate x and the range coordinate r can

https://doi.org/10.5194/nhess-2021-101
Preprint. Discussion started: 13 April 2021

Natural Hazards and Earth System Sciences
Discussions

be expressed as (1):

$$\delta\phi_j = \phi_B(x,r) - \phi_A(x,r) \tag{1}$$

$$\approx \frac{4\pi}{\lambda}[d(t_B,x,r) - d(t_A,x,r)] + \Delta\phi^j_{topo}(x,r) + \Delta\phi^j_{APS}(t_B,t_A,x,r) + \Delta\phi^j_{noise}(x,r)$$

where $j\epsilon(1,\dots,M)$; λ is the centre wavelength of the signal; $d(t_B,x,r)$ and $d(t_A,x,r)$ are t_B and t_A, respectively, relative to $d(t_0,x,r)=0$, which is the cumulative deformation in the radar line of sight direction; $\Delta\phi^j_{topo}(x,r)$ represents the residual terrain phase in the differential interferogram; and $\Delta\phi^j_{APS}(t_B,t_A,x,r)$ is the atmospheric delay phase.

To obtain accurate deformation information of the deforming area, the residual phase of the terrain and the atmospheric delay phase need to be removed. After removing the residual terrain phase and atmospheric delay phase and ignoring the noise phase, equation (2) can be expressed as:

$$\delta\phi_j = \phi_B(x,r) - \phi_A(x,r) \approx \frac{4\pi}{\lambda}[d(t_B,x,r) - d(t_A,x,r)] \tag{2}$$

The phase in equation (2) is expressed as the product of the average phase velocity and time of the two acquisition times:

$$v_j = \frac{\phi_j - \phi_{j-1}}{t_j - t_{j-1}} \tag{3}$$

The phase of the j-th interferogram can be expressed as:

$$\sum_{k=t_{A,j}+1}^{t_{B,j}}(t_k - t_{k-1})v_k = \delta\phi_j \tag{4}$$

Equation (4) is simplified to:

$$Bv = \delta\phi \tag{5}$$

Equation (5) represents an M×N matrix. The differential interferogram of the small baseline set adopts the multi-master image strategy. Therefore, matrix B is prone to rank deficit. Using the singular value decomposition (SVD) method, the generalized inverse matrix of matrix B can be obtained, and the minimum norm solution of the velocity vector can be obtained. Finally, the deformation variables of each time period can be obtained through the velocity integral in each time period.

To retrieve the temporal behaviour of landslide motion, we carried out time series InSAR analysis based on unwrapped interferograms. Our processing could be divided into three sections: topographic error (topo-error) removal, atmospheric phase screen (APS) removal and SBAS-InSAR analysis.

3.3.1 Topographic error (topo-error) removal

The accuracy of the DEM, that is, the accuracy of the estimation of the Earth's topography, is limited by the method and equipment used to generate the DEM, and the topography will change with time (Hu et al., 2017). When using the DEM to estimate the terrain phase, if there is an error in the DEM used, a terrain phase error term will remain in the interference phase, and the terrain phase error will affect the accuracy of the final deformation signal extraction. The terrain residual phase caused by the external DEM can be expressed as:

$$\Delta\phi^j_{topo}(x,r) = \frac{4\pi}{\lambda}\frac{B_\perp \Delta z}{r\sin\theta} \tag{6}$$

Δz represents the DEM error, and $B_\perp$ represents the vertical baseline. Equation (6) shows that the DEM error phase is related to the vertical baseline of the interference pair, the radar wavelength, and the vertical baseline distance.

3.3.2 GACOS atmospheric correction

Conventional InSAR time series analysis methods assume that atmospheric errors are temporally random, with only the spatial

https://doi.org/10.5194/nhess-2021-101
Preprint. Discussion started: 13 April 2021


Natural Hazards and Earth System Sciences
Discussions

correlation considered. However, the time dependence of atmospheric errors should not be ignored because the water content of the troposphere varies with the seasons and atmospheric errors are also related to topography. The generic atmospheric correction online service (GACOS) (Yu et al., 2018, 2017) can reduce the long wavelength of a single interferogram and the atmospheric errors related to the terrain (Figure 8).

GACOS incorporates model level surface pressure, temperature, and specific humidity from the High-Resolution European Centre for Medium Weather Forecasts (HRES-ECMWF) numerical weather model to calculate atmospheric delays at each 0.125-degree grid point spatially (i.e., a spacing of approximately 9-12 km) and 6 h temporally. Because the acquisition time of the SAR images differs from that of the HRES-ECMWF data, simple linear temporal interpolation is applied. Our hypothesis is that successful individual interferogram atmospheric correction leads to a reduction in the atmospheric spatial-temporal correlation within a stack of interferograms. The residual short-wavelength atmospheric errors are then filtered out by an APS filter, and the displacement time series is estimated by the tabu search (TS) algorithm.

4 Results

The deformation results from Sentinel-1A/B data are obtained by using the algorithm described in Section 2. We investigate how the deformation is distributed spatially and evolves over time. Figure 9 shows that the deformation is mainly concentrated on the right side of the viewing angle and centred on the landslide body. The red line represents the clearly identifiable boundary of the landslide body. The geocoded deformation rate results are superimposed on a Landsat-8 image in Figure 9. A negative value of the deformation rate indicates that the deformation point moves away from the satellite sensor, and a positive value indicates that the deformation point moves towards the satellite sensor. The results of the InSAR view-direction deformation analysis show that the deformation values in Figure 9 are all negative, indicating that the landslide body slides downwards towards the Jinsha River as a whole, which conforms to the sliding law of a landslide body. The figure illustrates that strong deformation of the landslide is located in the middle part and the front edge of the landslide. We selected three representative points (P1-P3) for the locations of the largest local deformation rates in Figure 9 and analysed the deformation characteristics of these points over time in Figure 10. All the deformation characteristics are coincident, and the maximum cumulative deformation of point 1 (P1) is approximately 200 mm. Figure 10 shows that there is a clear acceleration trend in deformation at each point, which may be caused mainly by precipitation. The particular causes of the deformation are discussed in Section 5 for specific analysis.

5 Discussion

5.1 Comparison of InSAR and GNSS observations

Any kind of surface deformation can be regarded as composed of three directional components: east, north, and up (E, N, and U). Assuming that the east-west, vertical, and north-south deformations measured by GNSS are d_{E-GPS}, d_{N-GPS} and d_{U-GPS}, respectively, the model of $d_{LOS-GPS}$ can be expressed as:

$$d_{LOS-GPS} = d_{U-GOS}cos\theta - sin\theta[d_{N-GPS}\cos\left(\alpha - \frac{3\pi}{2}\right) + d_{E-GPS}\sin\left(\alpha - \frac{3\pi}{2}\right)] \quad (7)$$

θ is the incident angle of the radar side view observation, and α is the angle between the flight direction of the radar satellite and the direction of true north. According to equation (7), the three-dimensional deformation measurements at the three GNSS stations can be projected to the line of sight (LOS) direction of the satellite, and the comparison results with the corresponding

https://doi.org/10.5194/nhess-2021-101
Preprint. Discussion started: 13 April 2021


Natural Hazards and Earth System Sciences Discussions

InSAR timing are shown in Figure 12. From the figure, we can see that there is a certain difference between the SBAS LOS deformation results and the GNSS LOS deformation results, mainly due to the following issues. 1) Inconsistent resolution. The resolution of the SBAS result is 30 m, and the GNSS points cannot correspond to it one-to-one. 2) Cumulative error. There are certain errors in the GNSS and InSAR results, causing cumulative errors. However, from the figure, we can find that the two sets of results have a clear accelerating trend in the rainy season and that they are stable in the non-rainy season.

5.2 Spatial deformation of the landslide

The field engineering geological survey and related data show (Feng et al., 2020) that the landslide body can be divided into the front landslide area (B1, B2, B3 and B4) and the central front shallow landslide area (H1, H2 and H3) (Figure 13). The accumulation body of the Woda landslide faces the river front, with a steep slope and multiple surface landslides. The B1 collapse area is located on the upstream front edge of the ancient landslide accumulation body. The slope angle is steep, and there are steep landslide ridges at the rear edge. Some high-elevation rock masses in this area fall onto the river bank and accumulate on a gentle slope (Figure 14(a)). The B2 collapse area is located at the front edge of the ancient landslide accumulation body, and the slope angle is relatively steep. In this area, local high-elevation rock masses slid down onto the river bank and accumulated on a gentle slope. The trees on the surface of the slope in the B1-B2 area are dense and grow normally, indicating that the rock and soil here are relatively stable. The B3 collapse area is located at the front edge of the ancient landslide accumulation body and slightly downstream. The slope surface is generally exposed bedrock, the top of the slope is covered with a thin soil, and the slope is steep (Figure 14(b)). There are almost no trees growing in this area, and the rock layers are slightly inclined to the slope, which is not conducive to sliding; however, joints and fissures develop along the slope, which is conducive to the occurrence of small-scale rock collapses. From this situation, small-scale landslides of surface rock and soil can be inferred to have occurred continuously. The B4 collapse zone is located at the front edge of the downstream side of the ancient landslide accumulation body. The rear edge of the collapse body develops a number of tensile fractures, which are generally arc-shaped, and the widths of the fractures vary from 5 to 30 cm (Figure 14(c)). The lower part of the area is bedrock, which dips into the slope and limits the scale of landslides. The H1 collapse area is located in the middle and rear parts of the slope. The sliding direction of the landslide is basically the same as that of the slope. The scale is small. The landslide material is the surface soil with little gravel and no large rocks (Figure 14(d)). H2 is located in the middle and front parts of the downstream section of the entire ancient landslide accumulation body, and there are many intermittent surface cracks in the back edge (Figure 14(e)). At H3, the landslide body is located in front of the downstream part of the entire ancient landslide accumulation body, very close to the H2 landslide, and the scope is small (Figure 14(f)). There are tiny surface cracks on the rear edge. On the lower slope, trees show no abnormal growth (skew, etc); thus, the lower rock and soil outside the range are speculated to be basically stable.

5.3 Analysis of landslide deformation factors

In this study, the rainfall around the landslide is compared with the LOS deformation results from GNSS and InSAR, as shown in Figures 11 and 12, respectively. To express the correlation, the concept of the Pearson correlation coefficient is introduced (Adler et al, 2010; Monedero et al., 2012; Dorogovtsev et al., 2010). The Pearson correlation coefficient is a quantity used to express the degree of linear correlation between the research variables, and its mathematical expression is shown in equation (8):

$$r(X,Y) = \frac{Cov(X,Y)}{\sqrt{Var[X]Var[Y]}} \quad (8)$$

https://doi.org/10.5194/nhess-2021-101
Preprint. Discussion started: 13 April 2021

where Cov stands for covariance and Var stands for variance. The Pearson correlation coefficients between rainfall and GNSS deformation results are calculated by equation (8), and the correlation coefficients are 0.1724922, 0.7583247 and 0.8622451. The GNSS01 point is located at the edge of the deformation zone, and its correlation coefficient is low. For the deformation results along the InSAR LOS, the correlation coefficients between Figure 15 (absolute value) and rainfall are 0.9490096, 0.9033602 and 0.9509995. The deformation results (GNSS03, GNSS05, P2, and P3) can pass the 0.01 confidence level significance test and show that the rainfall and the changes in the deformation results agree well with each other. This correspondence proves the consistency of the relative relationship between rainfall and deformation results. According to the field investigation, the highest elevations to which the Jinsha River water level fluctuates where the landslide is located are 2930-2950 m, while the elevations of the landslide deformation zone are 3220-3580 m, which quite different from the Jinsha River water level fluctuations. Therefore, it can be inferred that the deformation area of the landslide is not directly related to the Jinsha River. The results of field investigations and related phenomena also imply that the slump was caused by concentrated precipitation. For example, in area B1 (Figure 14(a)), the range of skewed trees is located at the mouth of the gully on the slope, indicating that the deformation is caused by concentrated precipitation. In summary, the deformation of the Woda landslide is mainly due to movement caused by concentrated heavy rainfall.

5.4 Risk analysis of the landslide body

From the observation of the opposite bank of the landslide and the occurrence of exposed bedrock in the lower part of the downstream side of the landslide body, the block of lower bedrock is not conducive to the occurrence of large-scale deep landslides (Feng et al., 2020). From several drilled cores, the thickness of the mixed loose deposits of surface soil and rock is not particularly great, and the deposits are unevenly distributed; the two springs that developed on the landslide body are exposed because of the water-blocking effect of the bedrock. The corresponding bedrock depth is not very great. The shallow depth of the rock mass implies to a certain extent that the amount of soil mass to produce landslides is limited and that large-scale landslides are not very likely to occur. Based on the sliding instability and the structural characteristics of the slope rock mass in recent years, this landslide is mainly a small-scale landslide in which superficial rock and soil move under the action of rainfall. The gradual collapse of voids is mostly limited to the landslide body, and the surface materials will not directly enter the river; only the part of the shallow rock and soil near the front edge may slide directly into the river, but the sizes of individual slumps are limited. According to on-site visits and investigations, although the front edge of the landslide is steep, most of the landslides have accumulated for more than a year. In recent years, there has not been a large-scale landslide, only small-scale landslides. The landslide is located in the Jiangda structural belt, with strong structural activity in multiple periods of history. The rock mass is fragmented locally and has cracks along the slope. Therefore, the front bedrock may also collapse and fall on a small scale.

In general, large-scale landslides are considered unlikely to occur in the natural state, and small-scale landslides in the shallow surface layer are the manifestation. However, given the influence of extreme external conditions such as heavy rainfall and earthquakes, as well as the destruction of the integrity and strength of rock masses caused by strong tectonic movements of bedrock, the possibility of concentrated sliding and sudden large-scale collapse of deep shear bedrock caused by an overall large-scale instability in the soil-rock mixture on bedrock cannot be ruled out.

6 Conclusion

Based on space-borne SAR deformation observations from July 4, 2018, to August 29, 2020, the deformation characteristics

https://doi.org/10.5194/nhess-2021-101
Preprint. Discussion started: 13 April 2021

Natural Hazards and Earth System Sciences Discussions

of the landslide were analysed. To identify the boundaries and deformation distributions of the unstable areas, the results of space-borne SAR and field surveys were combined, and the spatial deformation characteristics and time evolution of the landslide were analysed. The factor inducing landslide deformation is concentrated heavy rainfall.

The research results show that SAR/InSAR technology can reveal the surface deformation of a landslide body and characterize the active stage and development trend. This work also indicates that InSAR technology has broad applicability to early warning systems and monitoring of geological disasters in problematic mountainous areas. These prospects provide new ideas for similar landslide monitoring and early warning systems.

Data availability

The Sentinel-1A/B SAR images were downloaded from the Sentinel-1 Scientific Data Hub (http://scihub.copernicus.eu).

Author contributions

BL and JW designed the general idea and wrote the text; WJ contributed to paper writing and revision; YL was the chief technical director; WY, QL and JQ processed the GPS and InSAR data; and QH, QZ, ZZ and ZJ contributed to paper writing. All authors discussed the editors' opinions and revised the paper.

Competing interests

The authors declare that they have no conflict of interest.

Financial support

This work was supported by a research grant from National Institute of Natural Hazards, Ministry of Emergency Management of China (ZDJ2019-17).

Acknowledgements

The figures were generated using the Generic Mapping Tools software (Wessel et al., 2013). Many thanks to Professor Tao Li, Aichun Liu and Yiming Liu, who also took part in the field investigation of the Woda landslide.

References

Adler, J., and Parmryd, I.: Quantifying colocalization by correlation: the Pearson correlation coefficient is superior to the Mander's overlap coefficient. Cytometry Part A, 77(8): 733-742, https://doi.org/10.1002/cyto.a.20896, 2010.

Bayer, B., Simoni, A., Schmidt, D., and Bertello, L.: Using advanced InSAR techniques to monitor landslide deformations induced by tunneling in the Northern Apennines, Italy. Engineering Geology, 226: 20-32, https://doi.org/10.1016/j.enggeo.2017.03.026, 2017.

Cannon, S. H., Kirkham, R. M., and Parise, M.: Wildfire-related debris-flow initiation processes, Storm King Mountain, Colorado. Geomorphology, 39(3-4): 171-188, https://doi.org/10.1016/S0169-555X(00)00108-2, 2001.

Chen, H. Q., Xu, Y. Q., Zuang, M. G., Jiang, Z., and Zhang, N.: Analysis on the basic problems of the construction of geological disaster emergency support system. Chinese Journal of geological hazards and Prevention. 22(04): 108-111,

https://doi.org/10.5194/nhess-2021-101
Preprint. Discussion started: 13 April 2021

https://doi.org/10.16031/j.cnki.issn.1003-8035.2011.04.024, 2011.

Deng, Q. D., Zhang. P. Z., Ran, Y. K., Yang, X. P., Min, W., and Chu Q. Z.: Basic characteristics of active tectonics of China. Science Chin, 32: 1020–1030, 2002.

Dorogovtsev, S. N., Ferreira, A. L., Goltsev, A. V., and Mendes, J. F. F.: Zero Pearson coefficient for strongly correlated growing trees. Physical Review E, 81(3): 031135, 2010.

Feng, W. K., Dun, J. W., Yi X. N., and Zhang, G. Q.: Deformation analysis of Woda village old landslide in Jinsha River basin using SBAS-InSAR technology. Journal of Engineering Geology, 28(2): 384-393, https://doi.org/10.13544/j.cnki.jeg.2019-411, 2020.

Guan, Z., and Li, Z.: Characteristics of geological disasters in Changdu, Tibet and Countermeasures for prevention and control. Chinese Journal of geological hazards and prevention, 29 (02): 104-107, https://doi.org/10.16031/j.cnki.issn.1003-8035.2018.02.17, 2018.

Highland, L., and Bobrowsky, P. T.: The landslide handbook: a guide to understanding landslide. Reston: US Geological Survey, US, 2008.

Hooper, A.: A multi−temporal InSAR method incorporating both persistent scatterer and small baseline approaches. Geophysical Research Letters, 35(16), https://doi.org/10.1029/2008GL034654, 2008.

Hu, X., Wang, T., Pierson, T. C., Lu, Z., Kim, J., and Cecere, T. H.: Detecting seasonal landslide movement within the Cascade landslide complex (Washington) using time-series SAR imagery. Remote Sensing of Environment, 187: 49-61, http://dx.doi.org/10.1016/j.rse.2016.10.006, 2016.

Hu, X., Lu, Z., Wang, T., Pierson, T. C., Kim, J., and Cecere, T. H.: Time-series InSAR analysis of Cascade landslide complex, Washington, USA, 2017.

Iverson, R. M.: Landslide triggering by rain infiltration. Water resources research, 36(7): 1897-1910, 2000.

Malamud, B. D., Turcotte, D. L., Guzzetti, F., and Reichenbach, P.: Landslides, earthquakes, and erosion. Earth and Planetary Science Letters, 229(1-2): 45-59, https://doi.org/10.1016/j.epsl.2004.10.018, 2004.

Monedero, I., Biscarri, F., León, C., Guerrero, J. I., Biscarri, J., and Millán, R.: Detection of frauds and other non-technical losses in a power utility using Pearson coefficient, Bayesian networks and decision trees. International Journal of Electrical Power & Energy Systems, 34(1): 90-98, https://doi.org/10.1515/ijeeps-2015-0206, 2012.

Li, Y. S., Jiao, Q. S., Hu, X. H., Li, Z. L., Li, B. Q., Zhang, J. F., Jiang, W. L., Luo, Y., Li, Q,. and Ba, R. J.: Detecting the slope movement after the 2018 Baige Landslides based on ground-based and space-borne radar observations. International Journal of Applied Earth Observation and Geoinformation, 84: 101949, https://doi.org/10.1016/j.jag.2019.101949, 2020.

Schlögel, R., Doubre, C., Malet, J. P., and Masson, F.: Landslide deformation monitoring with ALOS/PALSAR imagery: A D-InSAR geomorphological interpretation method. Geomorphology, 231: 314-330, https://doi.org/10.1016/j.geomorph.2014.11.031, 2015.

Sun, Q., Zhang, L., Ding, X. L., Hu, J., Li, Z. W., and Zhu, J. J.: Slope deformation prior to Zhouqu, China landslide from InSAR time series analysis. Remote Sensing of Environment, 156: 45-57, https://doi.org/10.1016/j.rse.2014.09.029, 2015.

Schulz, W. H., Kean, J. W., & Wang, G.: Landslide movement in southwest Colorado triggered by atmospheric tides. Nature Geoscience, 2(12): 863-866, https://doi.org/10.1038/ngeo659, 2009.

Simons, M., Rosen, P. A. Interferometric synthetic aperture radar geodesy,3: 339-395, https://doi.org/10.1016/B978-044452748-6.00059-6, 2007.

Yang, C. S., Zhang, Q., Zhao, C. Y., Wang, Q. L., and Ji, L. Y.: Monitoring land subsidence and fault deformation using the small baseline subset InSAR technique: A case study in the Datong Basin, China. Journal of Geodynamics, 75: 34-40, https://doi.org/10.1016/j.jog.2014.02.002, 2014.

Yu, H. Y., Balz, T., Luo, H., Liao, M. S., and Zhang, L.: GPU accelerated interferometric SAR processing for Sentinel-1 TOPS data. Computers & Geosciences, 129:12-25, https://doi.org/10.1016/j.cageo.2019.04.010, 2019.

Yu, C., Li, Z. H., and Penna, N. T.: Interferometric synthetic aperture radar atmospheric correction using a GPS-based iterative tropospheric decomposition model. Remote Sensing of Environment, 204: 109-121, https://doi.org/10.1016/j.rse.2017.10.038, 2018.

Yu, C., Penna, N. T., and Li, Z. H.: Generation of real-time mode high-resolution water vapor fields from GPS observations. Journal of Geophysical Research: Atmospheres, 122(3): 2008-2025, https://doi.org/10.1002/2016JD025753, 2017.

https://doi.org/10.5194/nhess-2021-101
Preprint. Discussion started: 13 April 2021

Natural Hazards and Earth System Sciences
Discussions

Yin, Y. P., Zheng, W. M., Liu, Y., Zhang, J. L., and Li, X. C.: Integration of GPS with InSAR to monitoring of the Jiaju landslide in Sichuan, China. Landslides, 7(3): 359-365, https://doi.org/10.1007/s10346-010-0225-9, 2010.

Zhou, H., Zhong, K., Tang, J., Shu, L., Liu, Z., Shi, Y., Zhao, C., and Yang, H.: Formation, evolution and mineralization of Jiangda structural belt in eastern Tibet. Acta Geologica Sichuan, 28(04): 276-282, https://doi.org/10.3969/j.issn.1006-0995.2008.04.004, 2008.

Zhao, F. M., Meng, X. M., Zhang, Y., Chen, G., Su, X. J., and Yue, D. X.: Landslide susceptibility mapping of karakorum highway combined with the application of SBAS-InSAR technology. Sensors, 19(12): 2685, https://doi.org/10.3390/s19122685, 2019.

Figures and Tables:

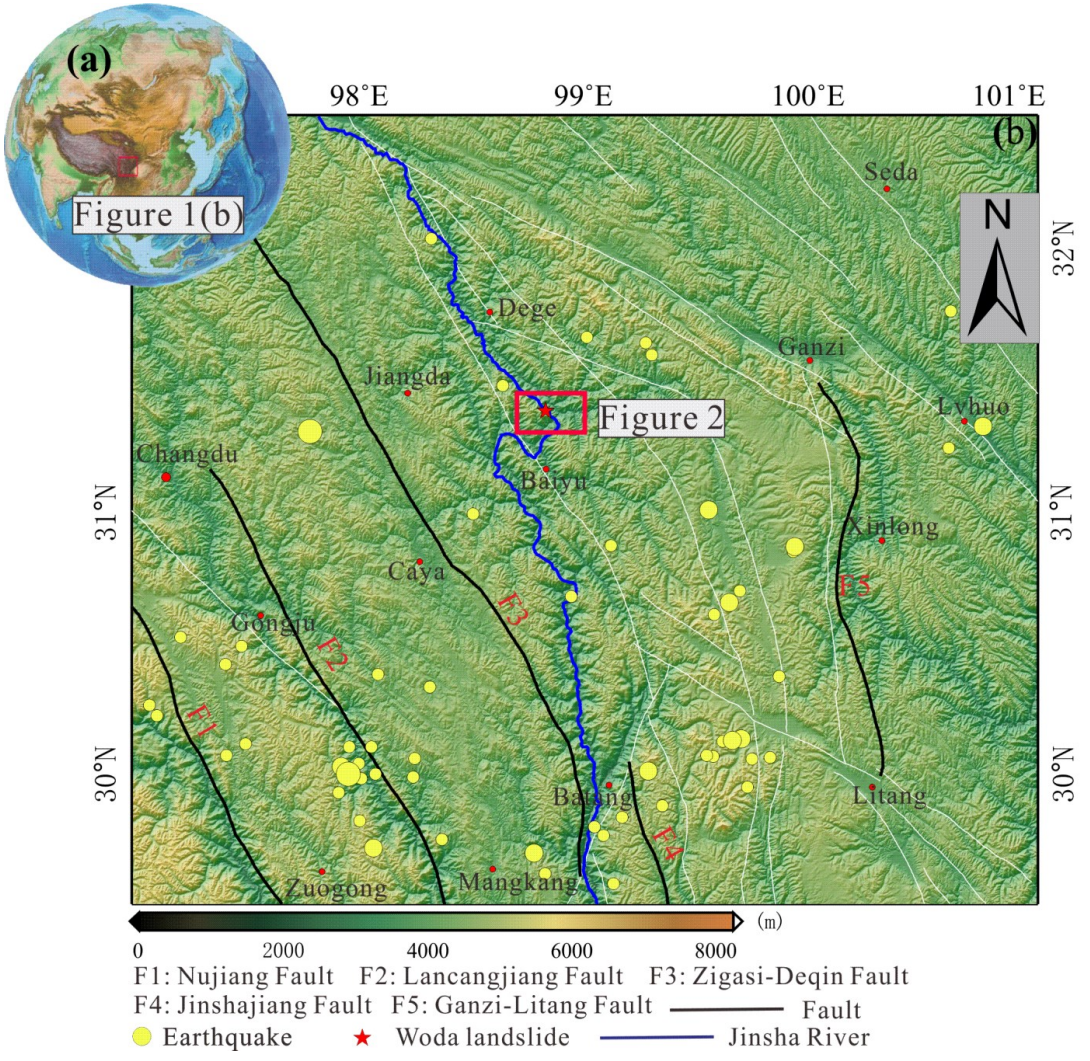

Fig. 1 The map shows the regional tectonics. The black lines represent 5 faults (modified from Deng et al. 2002). The white lines represent other faults. The yellow circles represent the locations of earthquakes (Mw ≥ 4.5) recorded by the USGS. The red star represents the location of the Woda landslide. A shuttle radar topography mission (SRTM) digital elevation model (DEM) is used as the base map.

https://doi.org/10.5194/nhess-2021-101
Preprint. Discussion started: 13 April 2021

Natural Hazards and Earth System Sciences
Discussions

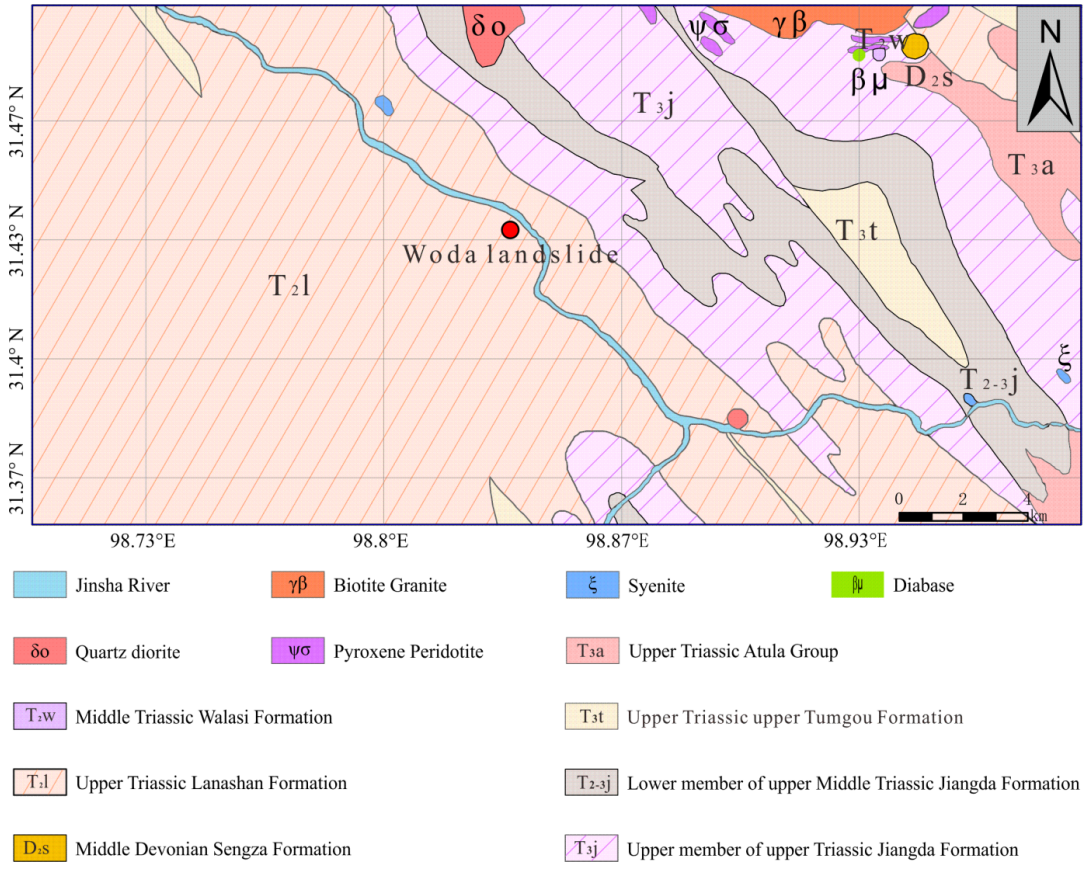

380 **Fig. 2 Regional geological setting of the Woda landslide (China Geological Survey 2014). The red circle represents the Woda landslide.**

https://doi.org/10.5194/nhess-2021-101
Preprint. Discussion started: 13 April 2021

Natural Hazards and Earth System Sciences
Discussions

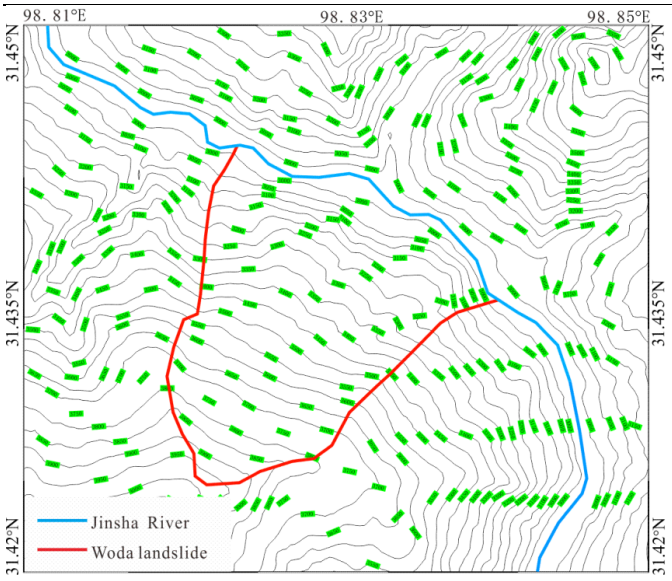

385 **Fig. 3 Contour lines surrounding the Woda landslide. The blue line represents the Jinsha River. The red line indicates the Woda landslide.**

Fig. 4 Multistage scarps developed in the middle and back parts of the landslide.

390

https://doi.org/10.5194/nhess-2021-101
Preprint. Discussion started: 13 April 2021

Natural Hazards and Earth System Sciences
Discussions

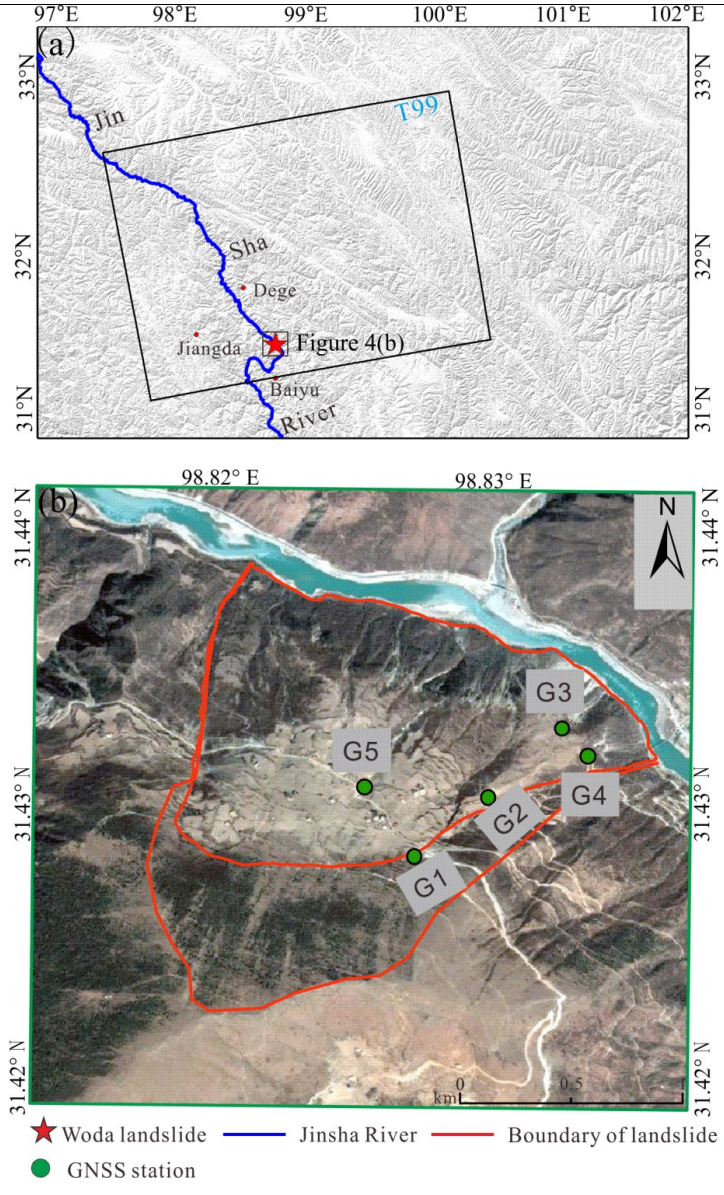

Fig. 5 InSAR Data coverage and GNSS locations. The dotted boxes represent the coverage of the Sentinel-1 images. The red star represents the location of the Woda landslide. The blue line indicates the Jinsha River. The red line marks the boundary of the landslide. The green circles indicate the GNSS stations.

395

https://doi.org/10.5194/nhess-2021-101
Preprint. Discussion started: 13 April 2021

Natural Hazards and Earth System Sciences
Discussions

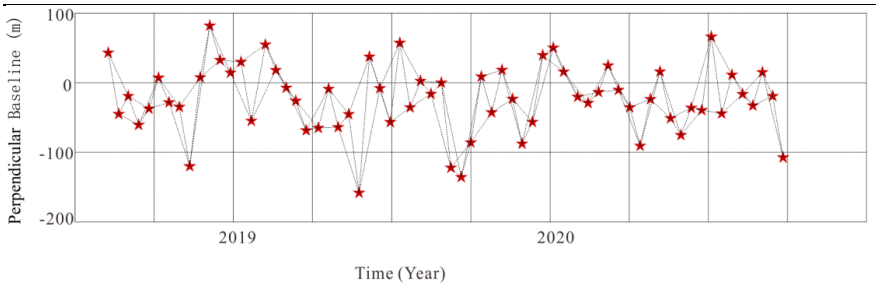

Fig. 6 Baseline network of interferograms from T99 datasets. The Y-axis shows the perpendicular baseline in metres. The imagery acquisition dates are represented in the format of YYYYMMDD. All the connecting lines represent interferometric pairs used for time series analysis. For T99, mean = 43.21 m, max = 158.04 m, and min = 2.43 m.

400

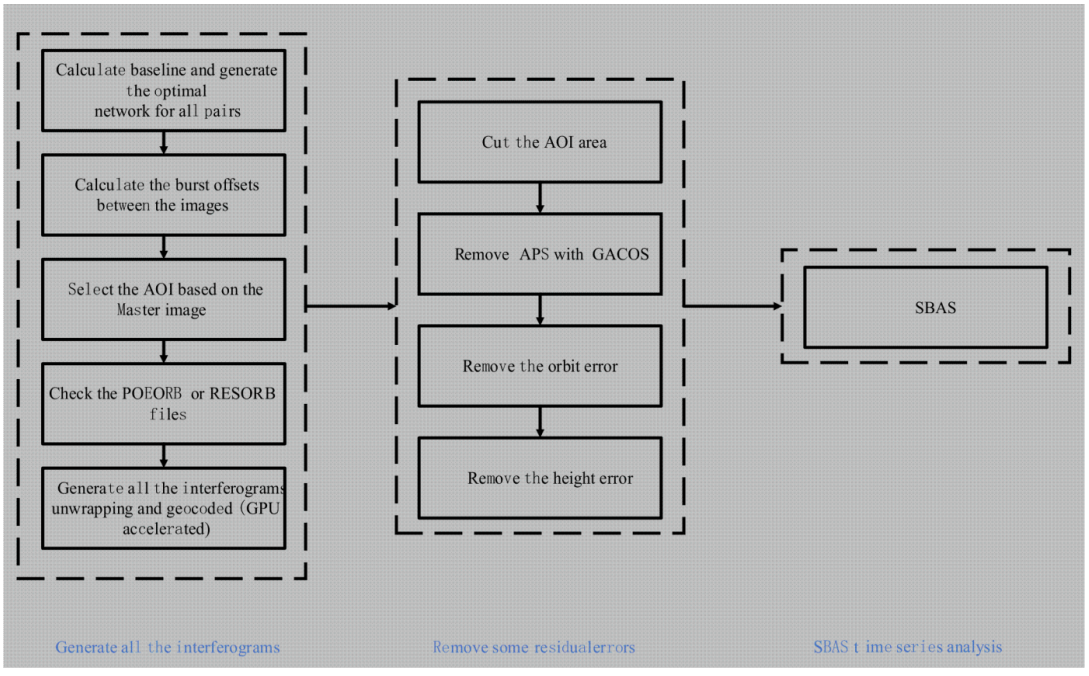

Fig. 7 Workflow of time series InSAR processing.

https://doi.org/10.5194/nhess-2021-101
Preprint. Discussion started: 13 April 2021

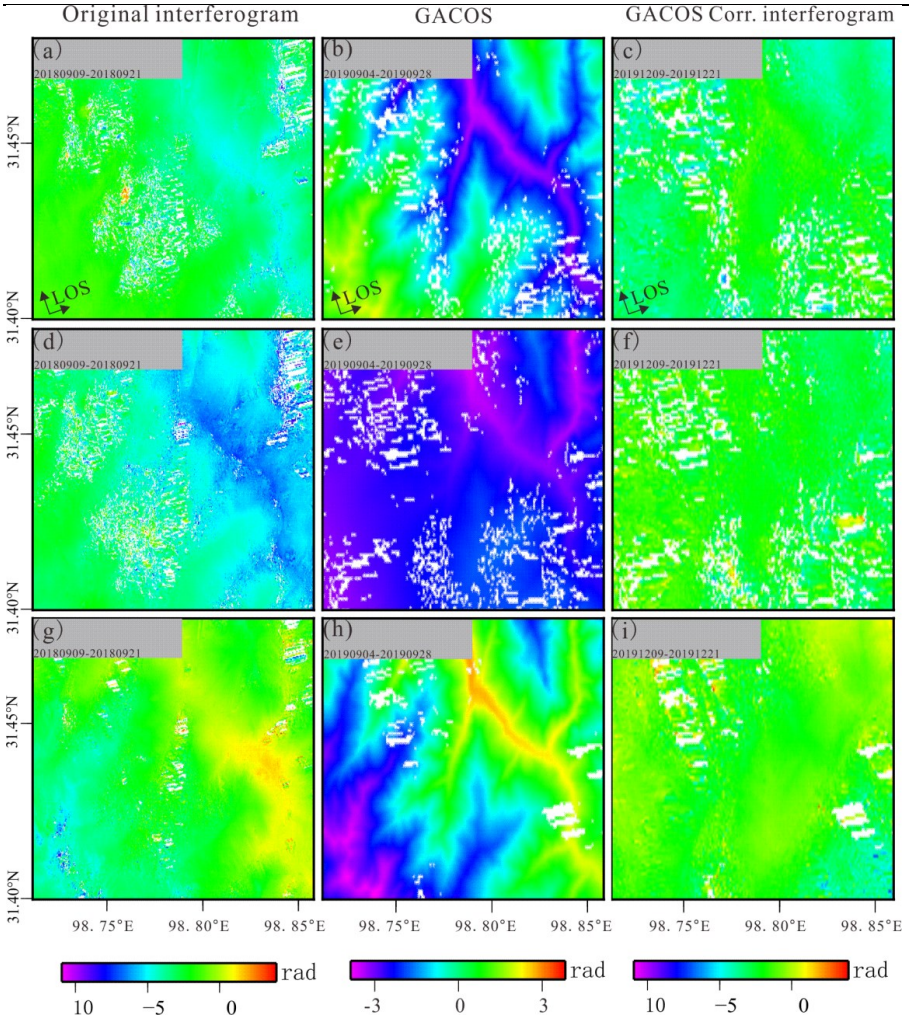

405 **Fig. 8 Atmospheric correction of the InSAR data using the GACOS software. (a, d, g) Original interferograms, (b, e, h) differenced wet delay maps along the line of sight (LOS) direction derived from GACOS, and (c, f, i) corrected interferograms.**

https://doi.org/10.5194/nhess-2021-101
Preprint. Discussion started: 13 April 2021

Natural Hazards and Earth System Sciences
Discussions

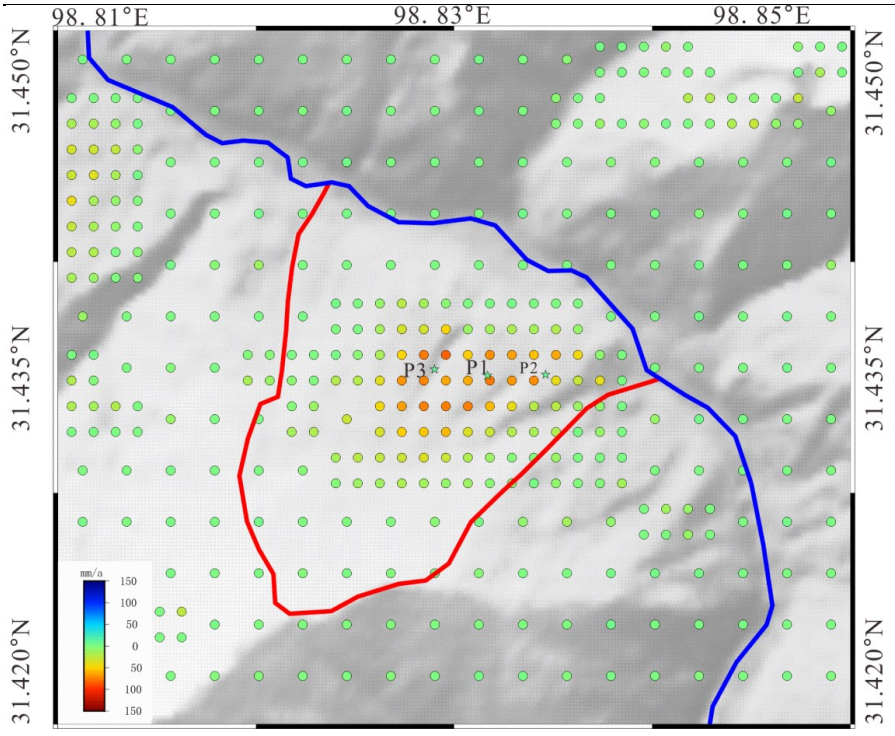

Fig. 9 LOS mean deformation velocity map from Sentinel-1 data for the period from July 4, 2018, to August 29, 2020. The red line represents the landslide region. The blue line indicates the Jinsha River. Three points (P1-P3) were selected for the time series in Fig. 10.

https://doi.org/10.5194/nhess-2021-101
Preprint. Discussion started: 13 April 2021

Natural Hazards and Earth System Sciences
Discussions

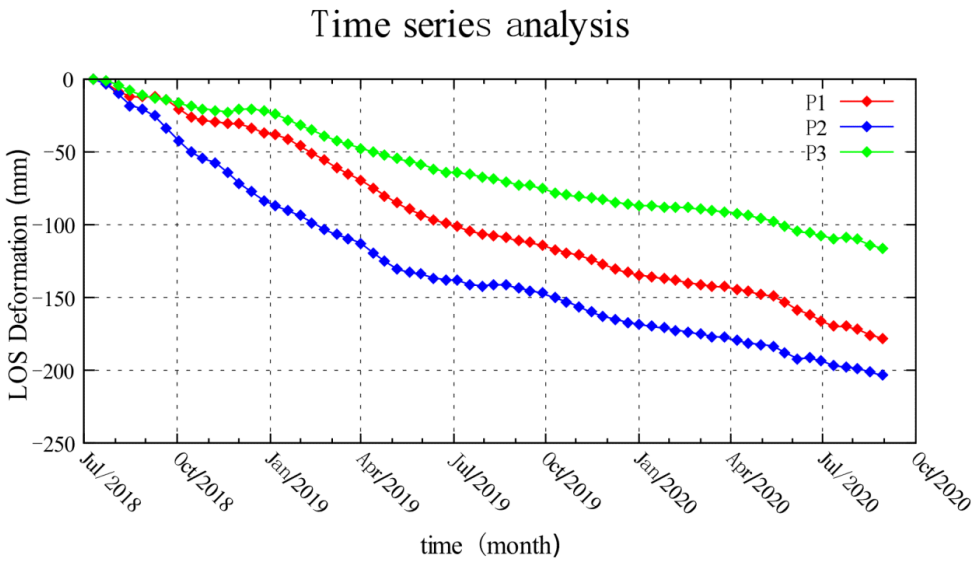

Fig. 10 Cumulative deformation of three points during the monitoring.

415

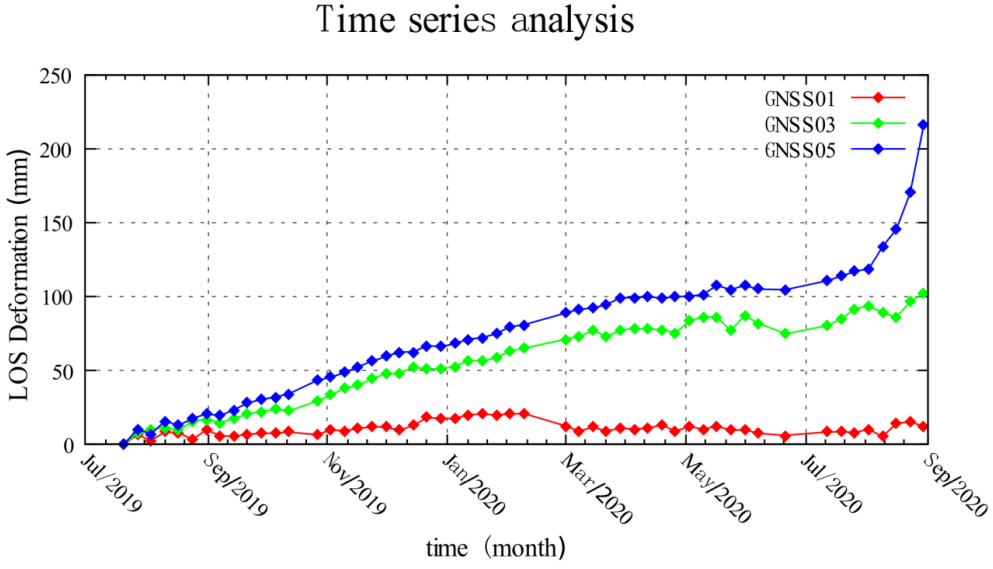

Fig. 11 Cumulative deformation at three GNSS stations during monitoring.

https://doi.org/10.5194/nhess-2021-101
Preprint. Discussion started: 13 April 2021

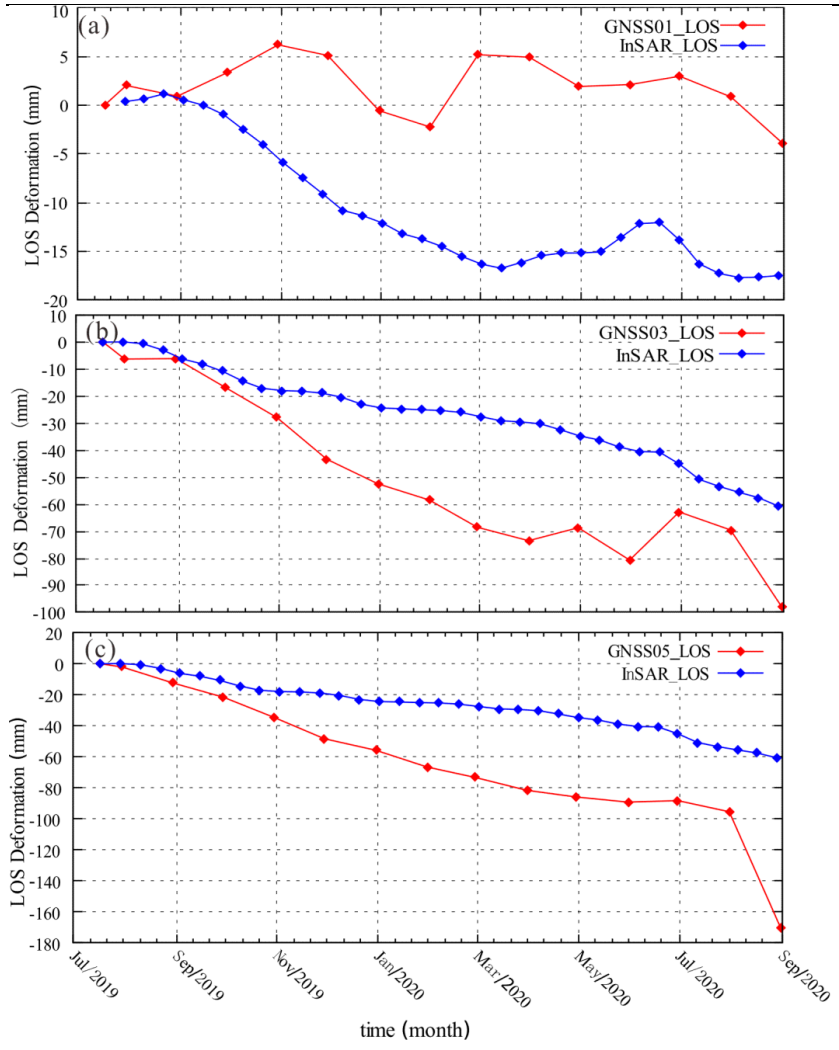

420 **Fig. 12 Comparison of LOS observation results for InSAR and GNSS.**

https://doi.org/10.5194/nhess-2021-101
Preprint. Discussion started: 13 April 2021

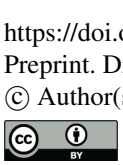

Natural Hazards and Earth System Sciences
Discussions

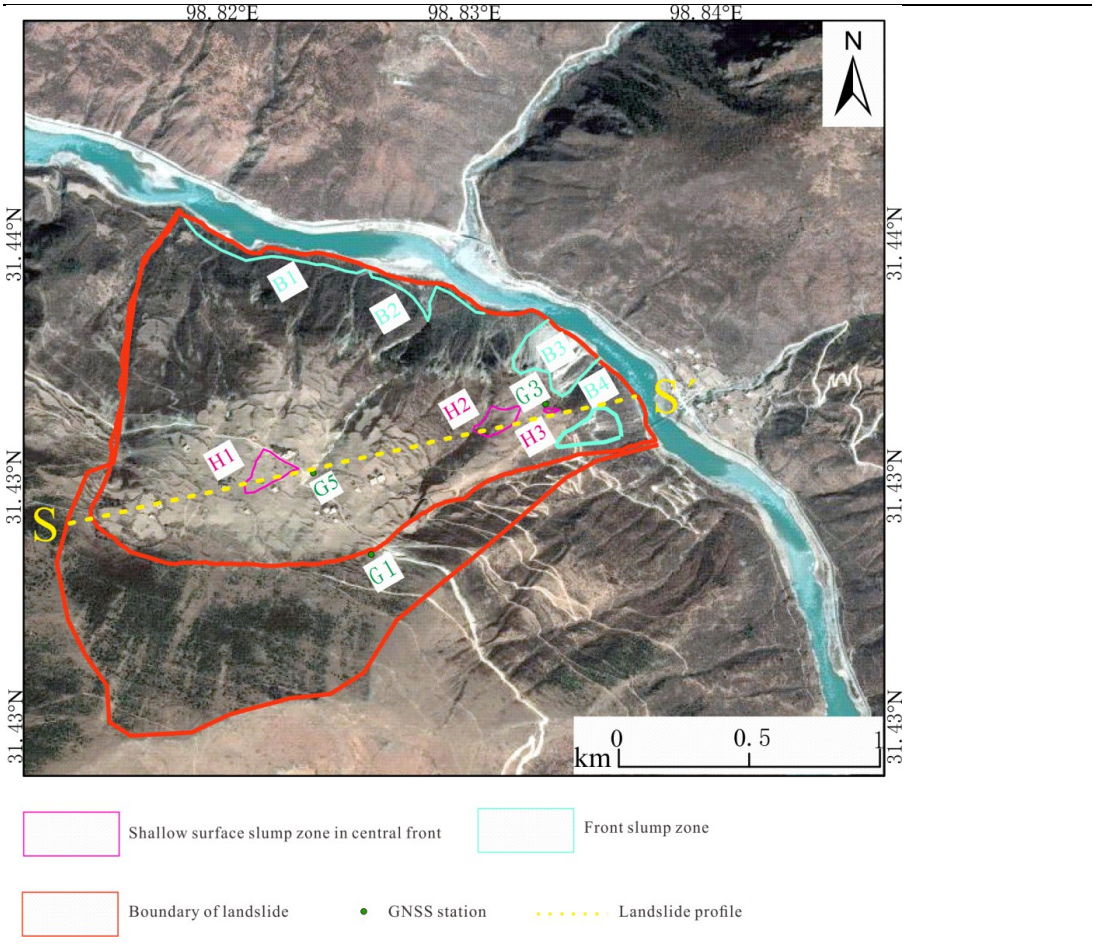

Fig. 13 Spatial deformation of the landslide. A Landsat-8 image is used as the base map. The green circle represents the GPS station. The red line represents the boundary of the Woda landslide. Spatial deformation of the landslide. A Landsat-8 image is used as the base map. The green circle represents the GPS station. The red line represents the boundary of the Woda landslide. The violet lines mark the middle and front parts of the landslide. The blue lines indicate the front of the landslide. The yellow dashed line represents the landslide profile. Gs label the locations of the GNSS stations. Bs indicate the front slump zone of the landslide. Hs represent the shallow surface slump zone in the central front.

https://doi.org/10.5194/nhess-2021-101
Preprint. Discussion started: 13 April 2021

Natural Hazards and Earth System Sciences
Discussions
Open Access
EGU

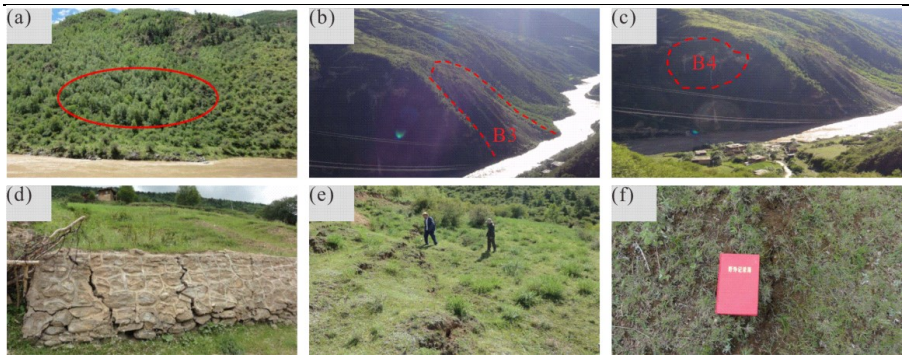

Fig. 14. Spatial deformation of the landslide. (a, b, c, d, e, and f) are photographs of B1, B3, B4, H1, H2, and H3, respectively.

https://doi.org/10.5194/nhess-2021-101
Preprint. Discussion started: 13 April 2021

Natural Hazards and Earth System Sciences
Discussions

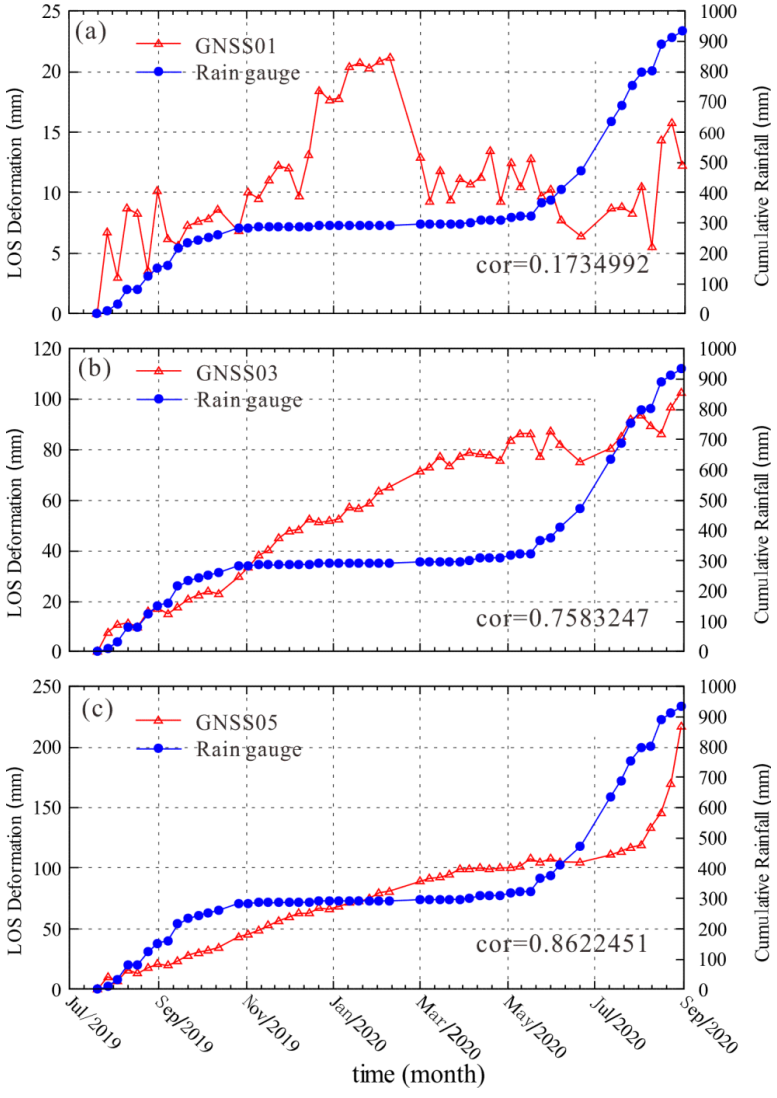

Fig. 15 Comparison between cumulative rainfall and GNSS LOS deformation.

https://doi.org/10.5194/nhess-2021-101
Preprint. Discussion started: 13 April 2021

Natural Hazards and Earth System Sciences
Discussions

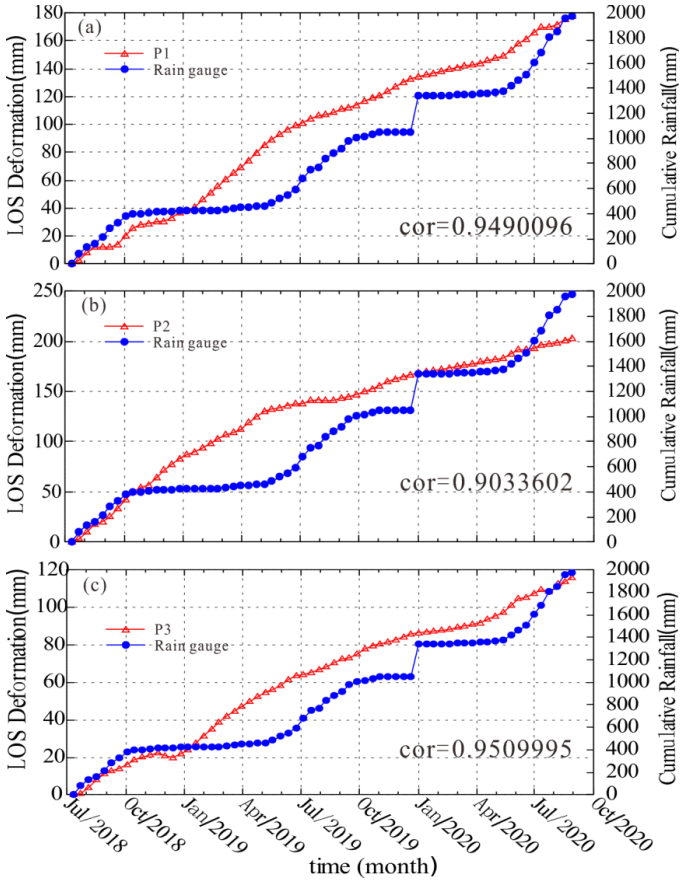

465

Fig. 16 Comparison between cumulative rainfall and InSAR LOS deformation.